



**HAL**  
open science

# The relation between Arctic sea ice surface elevation and draft: A case study using coincident AUV sonar and airborne scanning laser

Martin J. Doble, Henriette Skourup, Peter Wadhams, Cathleen A. Geiger

## ► To cite this version:

Martin J. Doble, Henriette Skourup, Peter Wadhams, Cathleen A. Geiger. The relation between Arctic sea ice surface elevation and draft: A case study using coincident AUV sonar and airborne scanning laser. *Journal of Geophysical Research. Oceans*, 2011, 116, 10.1029/2011JC007076 . hal-03502011

**HAL Id: hal-03502011**

**<https://hal.science/hal-03502011>**

Submitted on 1 Jan 2022

**HAL** is a multi-disciplinary open access archive for the deposit and dissemination of scientific research documents, whether they are published or not. The documents may come from teaching and research institutions in France or abroad, or from public or private research centers.

L'archive ouverte pluridisciplinaire **HAL**, est destinée au dépôt et à la diffusion de documents scientifiques de niveau recherche, publiés ou non, émanant des établissements d'enseignement et de recherche français ou étrangers, des laboratoires publics ou privés.

Copyright

## The relation between Arctic sea ice surface elevation and draft: A case study using coincident AUV sonar and airborne scanning laser

Martin J. Doble,<sup>1</sup> Henriette Skourup,<sup>2</sup> Peter Wadhams,<sup>3</sup> and Cathleen A. Geiger<sup>4</sup>

Received 28 February 2011; revised 22 July 2011; accepted 8 September 2011; published 16 November 2011.

[1] Data are presented from a survey by airborne scanning laser profilometer and an AUV-mounted, upward looking swath sonar in the spring Beaufort Sea. The air-snow (surface elevation) and water-ice (draft) surfaces were mapped at  $1 \times 1$  m resolution over a  $300 \times 300$  m area. Data were separated into level and deformed ice fractions using the surface roughness of the sonar data. The relation ( $R = d/f$ ) between draft,  $d$ , and surface elevation,  $f$ , was then examined. Correlation between top and bottom surfaces was essentially zero at full resolution, requiring averaging over patches of at least 11 m diameter to constrain the relation largely because of the significant error ( $\sim 15$  cm) of the laser instrument. Level ice points were concentrated in two core regions, corresponding to level FY ice and refrozen leads, with variations in  $R$  attributed primarily to positive snow thickness variability. Deformed ice displayed a more diffuse “cloud,” with draft having a more important role in determining  $R$  because of wider deformed features underwater. Averaging over footprints similar to satellite altimeters showed the mean surface elevation (typical of ICESat) to be stable with averaging scale, with  $R = 3.4$  (level) and  $R = 4.2$  (deformed). The “minimum elevation within a footprint” characteristic reported for CryoSat was less stable, significantly overestimating  $R$  for level ice ( $R > 5$ ) and deformed ice ( $R > 6$ ). The mean draft difference between measurements and isostasy suggests 70 m as an isostatic length scale for level ice. The isostatic scale for deformed ice appears to be longer than accessible with these data ( $>300$  m).

**Citation:** Doble, M. J., H. Skourup, P. Wadhams, and C. A. Geiger (2011), The relation between Arctic sea ice surface elevation and draft: A case study using coincident AUV sonar and airborne scanning laser, *J. Geophys. Res.*, 116, C00E03, doi:10.1029/2011JC007076.

### 1. Introduction

[2] Many previous studies have attempted to relate the geometrical properties of the top and bottom surfaces of sea ice. Motivation has variously included estimation of the ice thickness distribution for large-scale modeling [Maslowski and Lipscomb, 2003], assessment of loads for icebreaking ships and offshore structures [Timco and Weeks, 2010], the determination of roughness characteristics to determine wind and water drag coefficients for dynamics modeling [e.g., Andreas et al., 1993], sound scattering or the confinement of oil spills under ice [Wilkinson et al., 2007].

[3] Such detailed mapping has traditionally been an extremely laborious manual process. While top surface mapping can be carried out relatively easily using standard surveying and leveling procedures, surveying the undersurface (the ice draft) has required drilling of many (hundreds) of holes, then manually measuring the draft of each. Such efforts were the focus of several large-scale campaigns in the past, where many man years were expended [Weeks, 2010]. Efforts focused largely on pressure ridges [e.g., Davis and Wadhams, 1995; Kovacs et al., 1973], since these are the least constrained and generally most interesting features from the mechanics viewpoint, as they represent the strongest features of the ice cover. A summary paper [Timco and Burden, 1997] identified a total 176 ridges in the literature which had been “manually” profiled to date. Clearly, this total represents a vanishingly small sample of the typical variability of the Arctic ice cover.

[4] As in many walks of life, technology has now rendered this task less burdensome. Surface elevation can be rapidly mapped using an airborne scanning laser profilometer, which typically provides a 300 m wide swath under the aircraft at a resolution of  $1 \times 1$  m horizontally and 10–15 cm RMS vertically, while the aircraft flies at 250 kph. Large

<sup>1</sup>LOV, UMR 7093, UPMC, Université Paris 06, Observatoire Océanologique, Villefranche sur Mer, France.

<sup>2</sup>Division of Geodynamics, National Space Institute, Copenhagen Ø, Denmark.

<sup>3</sup>Department of Applied Maths and Theoretical Physics, University of Cambridge, Cambridge, UK.

<sup>4</sup>Geography Department, College of Earth Ocean and Environment, University of Delaware, Newark, Delaware, USA.

areas can thus be covered very quickly, though the data processing to remove aircraft motion and geoid surface is rather more time consuming. Underneath the ice, autonomous underwater vehicles (AUVs) are now beginning to be practical, using upward looking sonar (either interferometric or multibeam) to measure an approximately 100 m wide swath above the vehicle. Resolution is up to  $50 \times 50$  cm horizontally and 3 cm RMS vertically, giving an extremely detailed picture of under-ice features. The ideal survey would apply these two techniques to build a true coincident map of top and bottom surfaces.

[5] Earlier efforts toward this goal used (1) two-dimensional profiles using a manned submarine and P-3 aircraft [Comiso *et al.*, 1991; Wadhams *et al.*, 1992] and (2) an acoustically navigated ROV (with an upward looking single-beam sonar, giving widely separated measurements along discrete tracks as opposed to the “full coverage” obtained from multibeam sonar surveys) and surface leveling (points) to construct digital elevation maps of ice in the Beaufort Sea [Bowen and Topham, 1996; Francois, 1977; Melling *et al.*, 1993]. Previous AUV sonar deployments were reviewed in an earlier paper [Wadhams and Doble, 2008].

[6] The 2007 Applied Physics Laboratory Ice Station (APLIS) provided the first opportunity to carry out the long-imagined full 3-D coincident survey using AUV and scanning airborne laser. The camp was staged from 1 to 15 April in the Beaufort Sea north of Prudhoe Bay, Alaska, at approximately  $73^\circ\text{N}$ ,  $145^\circ\text{W}$ , in an area of dominantly 100% ice concentration, as seen by passive microwave satellites, though there were frequent small leads in the immediate area. The AUV measurements presented here were carried out on 12 and 13 April, with a single laser overflight occurring on 13 April. AUV operations at the site are detailed in previous publications [Doble *et al.*, 2009; Wadhams and Doble, 2008].

[7] The motivation for our study was primarily to examine the relation between draft  $d$  and surface elevation  $f$  over different ice types. Not enough is known about the detailed relation between these parameters at a time when the ratio, hereafter referred to as  $R = d/f$ , is becoming a critical parameter as we move toward spaceborne methods of determining ice thickness, such as ICESat and Cryosat-2. These altimetry techniques measure a small number (surface elevation) and multiply it by the poorly constrained  $R + 1$  to determine ice thickness. Clearly, such a technique implies significant errors if  $R$  is not well known, and  $R$  is far from being a single value. Most significant is its variation with snow thickness. Unfortunately, the only time this is less problematic, the summer, when all the snow masking the ice surface has melted, is also the time when radar altimeters cannot determine ice freeboard due to the presence of liquid water on the ice. The chosen ice and water densities also play a role, as does the prevalence of deformed ice, a mixture of ice types within the altimeter footprint and other important, radiometric, issues highlighted in recent work [Tonboe *et al.*, 2009, 2010].

[8] Early studies noted that the relation between surface elevation and thickness was best fitted using a thickness-dependent  $R$  [Ackley *et al.*, 1976]. Wadhams *et al.* [1992] determined  $R$  for multiyear ice in the central Arctic as  $7.9 \pm 0.6$ . They noted that the laser elevations under-

estimated the proportion of ice away from the mode (younger ice and ridged ice) while exaggerating the proportion close to the mode (3–6 m). The pattern was qualitatively explained with reference to the snow cover: thick ice can carry a relatively low snow load compared with thin ice, therefore very thin ice is transformed too thick, while very thick ice (thicker than the modal thickness) is transformed too thin, peaking the distribution. An elevation-dependent  $R$  value was therefore suggested. Spatial variability due to ice thickness was expected, with seasonal variability due to snow cover accumulation and melt. Forsstrom *et al.* [2011] found a value of  $5.0 \pm 1.5$  in the Fram Strait region in autumn. Investigations in the Lincoln Sea (north of Greenland) determined  $R$  as 5.3 for FY ice (implying 16 cm snow cover) and 4.7 for MY ice (44 cm snow cover) [Haas *et al.*, 2006]. They noted that any dependence of  $R$  with surface elevation needs to be tuned for ice type.

[9] The current paper discusses the instruments and methods used in this study, including detailed in situ measurements carried out at APLIS, which are used to constrain the values required to understand the  $R$  factor. We then calculate the point-to-point  $R$  value from the gridded laser and sonar data sets and examine its statistical properties. Deformed ice is defined by an innovative surface roughness classification method and then attention is focused on the contrast between the variation in  $R$  over level FY ice, the dominant ice type in this data set, and the deformed ice fraction. We examine how  $R$  varies with the measurement footprint size, simulating returns from the current and future satellite-borne altimeters, and finally investigate the dependence on ice type and footprint size of the mean difference between the measured ice draft and that predicted by isostasy, in search of an inherent isostatic scale in these data.

[10] Throughout the paper we refer to *surface elevation* as being the height above local sea level of the ice + snow composite, i.e., the surface measured by the laser. Though *freeboard* is commonly used in the same way, it is more correct to consider that term to relate only to the ice freeboard, not including the snow cover.

## 2. Data Acquisition

[11] The survey was centered on a first-year pressure ridge, which had been observed to form on 2 April 2007, shortly before the APLIS camp was established, and was thus poorly consolidated. The ridge divided a region of first year (FY) ice from a refrozen lead. Multiyear (MY) ice floes and FY rubble fields were also present in the area. The camp was located on one MY floe, 1 km distant from the study ridge.

### 2.1. Airborne Scanning Laser

[12] The ice-plus-snow surface elevation was surveyed on 13 April (coincident with the AUV sonar acquisition) using a Riegl LMS-Q140i-60 scanning laser profilometer mounted in a Twin Otter aircraft operated by Ken Borek Air Ltd. Data were collected as part of the larger National Space Institute (DTU Space) Spring 2007 campaign.

[13] The laser scanner measures with a horizontal resolution of  $1 \times 1$  m at a flight height of 300 m and a ground speed of 250 kph. The across-track swath width is roughly equal to the flight height. The vertical accuracy is in the order

of 10–20 cm depending primarily on errors in the kinematic GPS solutions, due to long baselines [Krabill *et al.*, 1995]. More information on the airborne instrumentation and the system setup is given by Hvidegaard *et al.* [2006].

[14] If the height of the sea surface is known, the surface elevation can be found directly from the measurements. Here, a geoid model is used as a first approximation of the sea surface height. However, due to tidal errors, ocean dynamic topography and measurement errors, it is necessary to implement a “lowest-level” filtering algorithm. The algorithm selects the lowest heights along the geoid-reduced laser measurements. These heights are assumed to be open water leads, or leads covered with thin ice, and are thus estimates of the instantaneous sea surface height. The distance between such points is typically 5 km, though in the area of the APLIS camp, numerous cracks or small leads were present. A smooth curve is fitted through the “lowest-level” points by using a least squares collocation (optimal estimation) function with correlation length 10 km and root-mean-square noise of 0.1 m. The resulting curve is an estimate of the instantaneous sea surface height, and the ice + snow surface elevation can be found accordingly [Hvidegaard *et al.*, 2006]. First results, using a similar method, are described by Hvidegaard and Forsberg [2002], where the absolute accuracy of the surface elevation is estimated to be in the order of 10–15 cm. The geoid model used in the processing is an updated Arctic geoid model, derived by spherical FFT methods from the Arctic Gravity Project terrestrial data [Forsberg and Kenyon, 2004] and GRACE satellite data. More details are given by Forsberg and Skourup [2005].

[15] The laser-derived surface elevation data were used as the reference frame for other measurements, since they were essentially synoptic over the widest area and georeferenced. Maximum observed surface elevation over the coincident area was 3.2 m and the median surface elevation was 46 cm. The probability distribution function was unimodal, with a 40 cm mode.

## 2.2. Under-Ice Swath Sonar

[16] Ice drafts were obtained using a Geoacoustics Geoswath 500 kHz interferometric sonar, mounted on a Gavia AUV, owned and operated by the manufacturers, then Hafmynd Ehf, now Teledyne Gavia Ehf. The vehicle was run inverted (i.e., rolled through 180°) and the sensors, normally configured to look downward at the seafloor, thus looked upward at the undersurface of the ice. A detailed description of the vehicle and sensors is given by Doble *et al.* [2009].

[17] The vehicle was run at depths between 20 and 30 m, to be sure of clearing the deepest ice features in the survey area, giving a usable sonar swath width of around 80 m (i.e., 40 m either side of the vehicle track). The vehicle was run tethered for safe and simple retrieval from the deployment hole, and thus only short missions were feasible. In all, 21 runs were performed, each consisting of an outward track up to 400 m from the hole, a wide turn and return to the hole. Missions were run in a star pattern, with the aim of achieving full coverage of the area out to a given radius, over the course of 2 days.

[18] Data were processed and binned to  $0.5 \times 0.5$  m, calculating a weighted mean of the values within each bin

using the *Geoswath Plus* software supplied by Geoacoustics. Bins typically contained 20 individual range-angle solutions, each with an estimated draft error of  $\pm 15$  cm. Error for binned values reduces by the square root of the number of contributions, giving  $\pm 3$  cm for draft error in a bin. Figure 1 shows the resulting mosaic of drafts rendered in three dimensions, with various ice types marked and with the probability density function (PDF) inset. Modal ice draft was 1.65 m, reflecting the dominance of level FY ice in the data set, with a secondary mode at 40 cm, due to refrozen leads. Maximum draft, attained in the FY ridge, was 16.8 m.

## 2.3. Coregistering Laser and Sonar Swaths

[19] The laser overflight was used as the “master map” to which each AUV sonar swath was matched. Features were identified on the laser surface elevation and on each sonar swath which could reliably be assumed to be collocated on their top and bottom surface, dominantly the edges of floes and refrozen cracks, which were numerous in this particular data set, as can be seen from Figure 1. Maps of the difference between scaled surface elevation and draft were plotted and the AUV swath translated and rotated to find the optimum match. AUV swaths which overlapped each other were checked for consistency once they were matched to the laser data. Sonar data was discarded if the optimum position from the consistency check differed from the laser-sonar match. This dominantly occurred following the turn for home at the furthest point of each line (i.e., mid mission) and we preferred straight tracks for the composite data set. We present data extracted from a total of eight runs (of 21 total). Multiple draft values from valid overlapping sonar swaths at any given location were averaged in the final mosaic. Over the critical area of the FY ridge, values of sonar draft (particularly the location of the deepest part of the ridge keel) were checked against a grid of 65 holes which were drilled in six lines across the ridge using Kovacs 2 inch diameter drill flights. These were located on the laser master map with reference to the AUV deployment hut, a 3 m high structure that was very obvious on the laser data, and to continuously recording GPS base stations installed in the camp command hut and at the end of survey lines.

[20] The matching process was iterative and time consuming, but essential to give confidence in any comparison between measurement types. Data match to the nearest pixel (i.e.,  $1 \times 1$  m) at the tie points. Between tie points, it is likely, given the struggles with AUV navigation detailed by Doble *et al.* [2009], that some misregistration occurs. It is expected that such hard-to-quantify positioning errors have a small impact on the study, however, since it is hardest to achieve a match over exactly those relatively homogenous regions where any misregistration will have the smallest effect. Consequently we feel justified in comparing the surface elevation and draft data sets at the highest resolution of  $1 \times 1$  m, though the majority of analysis presented here in fact takes place at larger scales (typically 11 m diameter patches).

## 2.4. In Situ Measurements of Snow, Ice, and Water Properties

[21] High-technology survey instruments, as used in this study, do not obviate the need for detailed surface measurements to establish the physical parameters of the site.

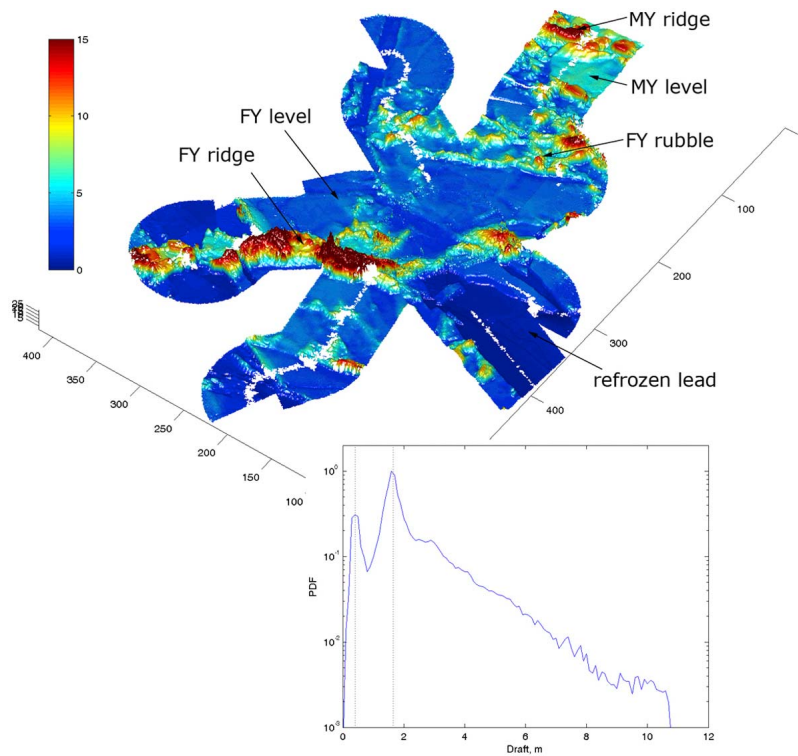


**Figure 1.** Three-dimensional view of the ice draft mosaic from eight runs of the AUV-mounted interferometric sonar. Axes and color bar are shown in meters, and examples of the various ice types in the image are shown with arrows. Gaps are present from acoustic shadowing and the poor returns at nadir over level ice from the interferometric sonar system. The PDF of the AUV data at  $1 \times 1$  m resolution (downscaled to the resolution of the coincident laser surface elevation data set) is shown in the inset. Modes at 0.40 m (refrozen leads) and 1.65 m (level FY ice) are marked as dotted lines.

Critical parameters in determining the  $R$  value are the density and thickness of the snow and ice and the surface seawater density. Extensive measurements of these were therefore made during the ice camp. Surface seawater density ( $\rho_w$ ) was calculated, from measurements made using a SeaBird 19 CTD lowered to a depth of 50 m, as  $1021 \text{ kg m}^{-3}$  (26 psu).

[22] A grid of 143 holes was drilled on level FY ice [see *Wadhams and Doble, 2008, Figure 1*] to ground truth the AUV sonar data at its first deployment site, approximately 2 km from the data presented here. Snow thickness was measured at 3 points around each hole, giving 429 measurements in total. Median snow thickness ( $h_s$ ) was  $11 \pm 9$  (Standard Deviation) cm. Snow density ( $\rho_s$ ) was  $240 \pm 16 \text{ kg m}^{-3}$ , from 12 snow samples distributed over the sampling area. Median ice draft ( $d$ ) was  $137 \pm 15$  cm, with an ice freeboard of  $13 \pm 5$  cm. From these measurements the in situ, or isostatic ice density ( $\rho_i$ ) is  $918 \pm 29 \text{ kg m}^{-3}$ . The measured region was far ( $>300$  m) from any deformed zones which might have disturbed its isostatic balance. Measured mean FY ice core density at the same site, from two side-by-side cores was 914 and  $920 \text{ kg m}^{-3}$ . This very close agreement suggests that the ice density measurement is reliable to better than  $10 \text{ kg m}^{-3}$  and is itself in very good agreement with isostasy, reflecting the very low porosity of the winter ice and the subsequent negligible drainage of fluids from the extracted core.

[23] Long transects were performed using a Geonics EM-31 electromagnetic induction device, with snow depths determined every five meters with a ruler. Six radial lines, centered on the ice camp itself, were performed, out to a distance of approximately 1000 m (C. A. Geiger et al., Impact of instrument footprint from electromagnetic induction sea ice thickness retrievals, submitted to *Journal of Geophysical Research*, 2011). In the area of the coincident measurements presented here (within 200 m of the ridge) the snow thickness was highly variable. Mean snow thickness was 27 cm, with a Standard Deviation of 29 cm. Maximum snow thickness was 1.19 m.

### 3. Comparing Draft and Surface Elevation

[24] We compare the surface elevations and drafts across the area covered by both laser and AUV measurements. AUV data were downsampled to the resolution of the laser data by taking the median value of the four  $0.5 \times 0.5$  m AUV bins contributing to each  $1 \times 1$  m laser bin. Total coverage of the coincident data set was  $87,500 \text{ m}^2$  of ice.

#### 3.1. Separating Deformed and Level Ice

[25] To understand the contributions to the observed top and bottom surface relations, it is useful to consider the deformed and level ice fractions separately. Deformed ice regions were identified by examining the surface roughness of the sonar data. A circular patch of 15 m diameter,

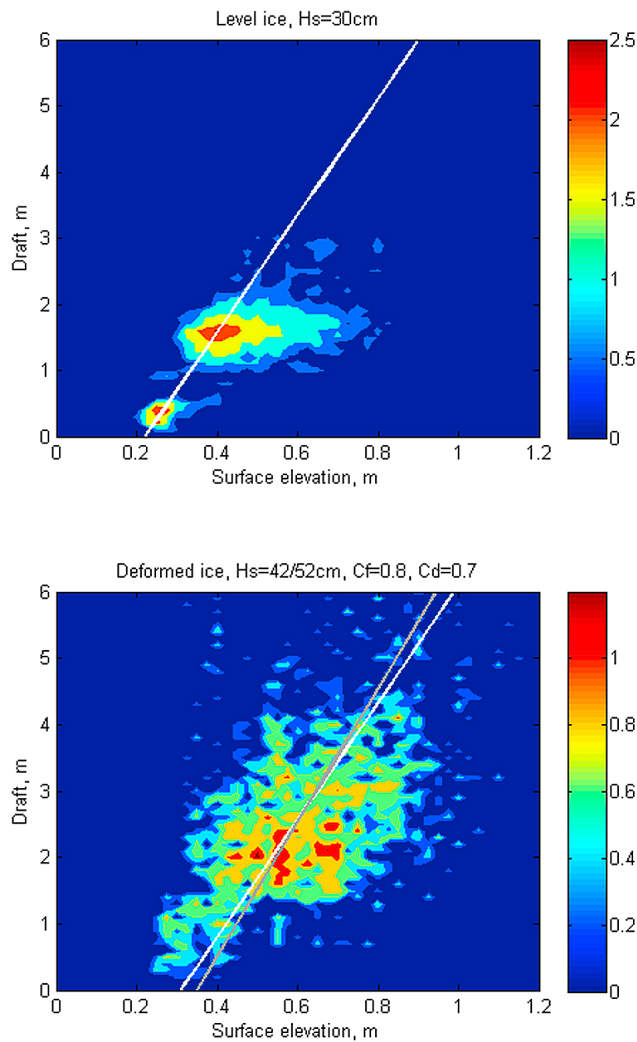


**Figure 2.** Contour plot of measured surface elevation against draft for (top) level ice and (bottom) deformed ice. Data are medians over 11 m diameter patches in both cases. The color scale shows the base 10 logarithm of the number of bins occupying each ⟨surface elevation–draft⟩ pairing. The inclined white line shows the modeled relation, given by equation (1), for the indicated fixed snow thicknesses. The deformed ice plot also shows the relation (gray) taking into account typical porosities for above- and below-water deformed ice features.

advancing in 1 m steps, was used to calculate the variogram (or semivariance) within the window [Webster and Oliver, 2007]. This patch size gives >100 bins per patch, a useful minimum figure to generate a representative variogram, while maintaining a reasonable resolution. In the sonar data presented here, variograms of deformed ice display peak magnitudes more than 100 times that of level ice, allowing them to be robustly segmented. The laser data is too noisy to classify in the same manner, however, and we use the sonar data to define “deformed” for both upper and lower surfaces. By this criterion, the coincident data set consists of 45% deformed ice by area, though this is likely to slightly overestimate the true deformed ice fraction, since the edges of level floes are also classified as deformed ice.

### 3.2. The ⟨Surface Elevation–Draft⟩ Relation

[26] Transforming the standard isostatic relation to relate ice draft,  $d$ , and ice + snow surface elevation,  $f$  (as measured by the laser) we obtain:

$$d = \frac{\rho_i f + h_s(\rho_s - \rho_i)}{\rho_w - \rho_i} \quad (1)$$

[27] If snow thickness and the various densities are constant, this gives a straight line relation between draft and surface elevation. At full resolution ( $1 \times 1$  m), however, the majority of ⟨surface elevation–draft⟩ pairings do not lie along the modeled relation: correlation between the parameters is effectively zero ( $r_S^2 = 0.07$ ; we quote Spearman’s Rank correlation,  $r_S$ , rather than the more familiar  $r^2$  since the data are not normally distributed, as is required for  $r^2$  to be correctly applied). Most points lie on the 1.65 m modal draft value, reflecting the dominance of FY ice in the data set, but these have a very wide spread of measured surface elevations, from 15 cm to over 1.4 m. A second horizontal band is seen at around  $d = 0.40$  m, representing the thin, refrozen lead areas, which display a similarly wide range of measured surface elevations.

[28] Averaging the draft and surface elevation over a larger area improves the correlation considerably. We form an approximately circular patch of a given diameter (an odd number of bins), and move this over the data (in both  $x$  and  $y$  directions) in half-radius steps, calculating the median value of draft and surface elevation within each patch. Though the value for a single patch is calculated as the median of bins within that patch, we only use bins within each patch which have been classified as level or deformed, according to the ice type under consideration.

[29] Figure 2 shows the results, for level and deformed ice fractions. Results are shown as a contour plot of  $\log_{10}$  (the number of points having a particular ⟨surface elevation–draft⟩ pairing) and mark the modeled relation given by equation (1). For level ice (Figure 2, top), a fixed snow thickness of 30 cm is marked: this intercepts the crossing of modal values and is close to the in situ mean measured figure. The relatively small patch of only 11 m diameter, chosen to mimic the expected footprint of the future ICESat-2 laser, increases the correlation between draft and surface elevation to  $r_S^2 = 0.70$ , collapsing the previously extended range of surface elevation values at the modal draft and refrozen leads to a far smaller range. These dominant ⟨surface elevation–draft⟩ pairings now lie close to the modeled line, though surface elevations are seen to be positively biased with respect to this line, suggesting positive snow thickness anomalies from the 30 cm value which intercepts the most common values.

[30] The contrast between full-resolution ( $1 \times 1$  m) and averaged ( $11 \times 11$  m) patches is explained by examining the histogram of the laser surface elevation data, which only displays a single mode at full resolution: the dominant level ice types are not resolved. Patch sizes of 11 m diameter and upward split the laser surface elevation histogram into two distinct modes, differentiating the refrozen lead (mode at 26 cm) from level FY ice (mode at 42 cm). We note that these two peaks are separated by almost exactly the stated RMS error of the laser instrument. Clearly the relatively

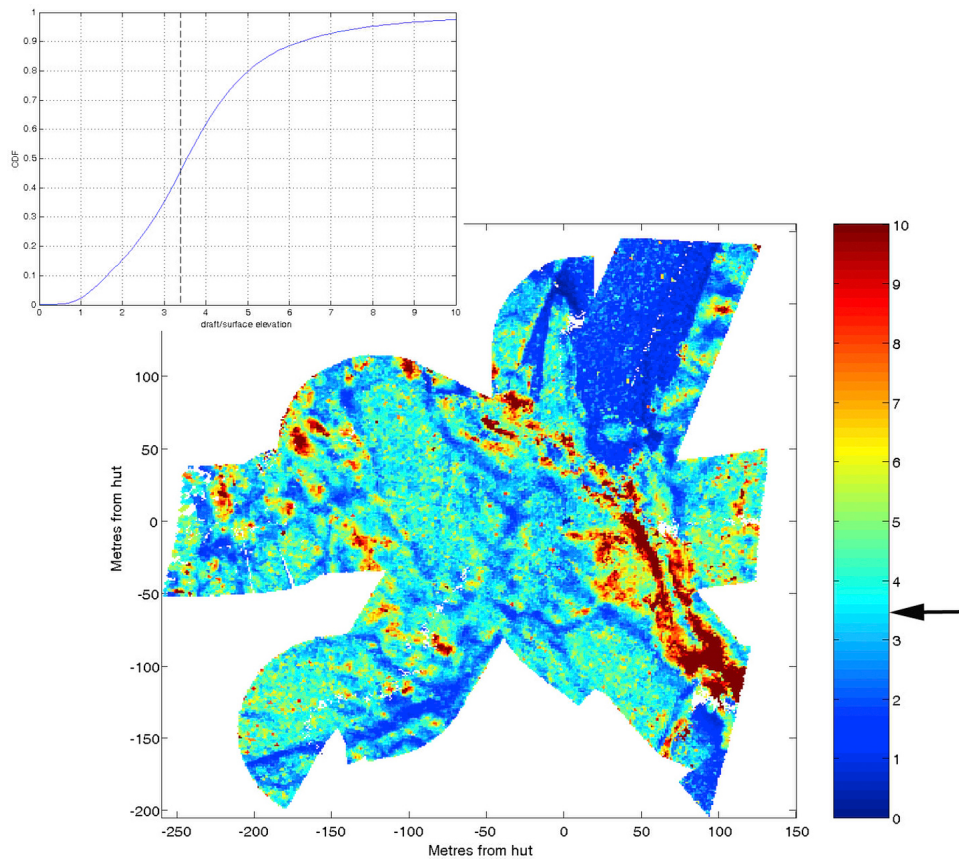


**Figure 3.** Map of  $R$  calculated at full resolution for all valid bins. The arrow next to the color scale marks the dominant (modal) level ice value of  $R = 3.4$ . Coordinates are referenced to the AUV deployment hole and hut. A relation with ice features is clear, with high values ( $\sim 10$ ) over ridge features and low values (1–2) over the thinnest ice, in refrozen leads. The inset curve shows the cumulative distribution function of the plotted  $R$  values, with the level ice value marked as a dashed line.

high noise of the laser instrument requires averaging if sufficient signal:noise ratio is to be obtained over such areas. The sonar drafts easily resolve the same ice types without further averaging, since (1) the accuracy has already been significantly increased by combining individual range-angle pairs into bins, inside the proprietary *GeoSwath* software, and (2) variations in the draft values are more pronounced than surface elevation, in line with isostasy.

[31] For the deformed ice fraction (Figure 2, bottom) we choose a fixed snow thickness which minimizes the total error to the fit line, defining  $\overline{\Delta d}$ , the mean draft error from the (isostatic) fit line:

$$\overline{\Delta d} = \frac{1}{N} \sum_f \sum_d \Delta d \cdot n_{f,d} \quad (2)$$

where  $n_{f,d}$  is the number of bins having any given value of surface elevation ( $f$ ) and draft ( $d$ ),  $\Delta d$  is the difference between the draft value under consideration and the draft value of the fit line at that surface elevation, and  $N$  is the total number of patches. For the  $11 \times 11$  m data shown, this gives zero error at 42 cm snow thickness (plotted as the white line in Figure 2 (bottom)). For the deformed ice fraction the effect of porosity was also investigated,

taking account of standard solid ice fractions above water ( $C_f = 0.8$ ) and below water ( $C_d = 0.7$ ) [Lepparanta and Hakala, 1992; Melling *et al.*, 1993]. Taking porosities into account, the zero  $\overline{\Delta d}$  value was achieved at 52 cm snow thickness, plotted as the gray line.

[32] The data form a much more diffuse “cloud” for deformed ice than for level ice. Since we have fitted the optimum snow thickness, the points lie symmetrically around the fit line, though we note that at low drafts the data are biased to a reduced snow thickness (to the left of the fit line). Evidently, 42 or 52 cm snow thickness is unlikely to exist on ice whose ice + snow surface elevation is less than these figures, in contrast to the Antarctic where negative ice freeboards are common.

[33] The spatial pattern of the major departures from point-to-point isostasy are shown in Figure 3, which plots  $R$  over the coincident region at full resolution (1 m bins). It is clear that the highest  $R$  values ( $\sim 10$ ) are associated with the FY ridge, where the sonar data show a much wider keel than the relatively thin sail seen by the laser. High values are also observed in other deformed ice areas, such as the FY rubble field and in the MY ridge. Conversely, the lowest values (1–2) are observed in the thinnest ice (refrozen leads), reflecting the relatively high contribution of snow

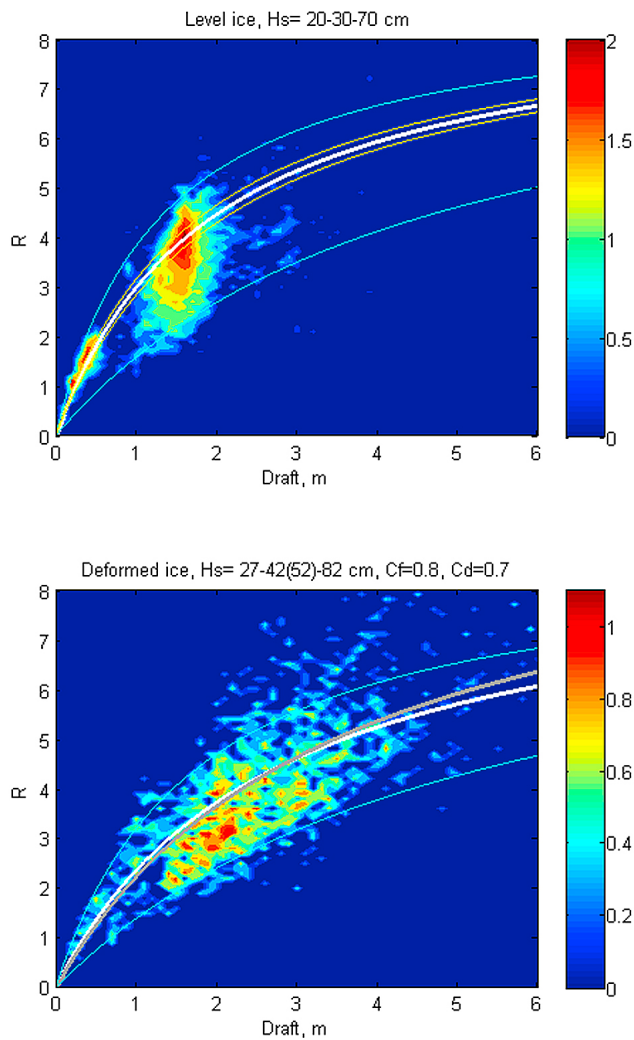


**Figure 4.** Contour plot of  $R$  against draft, compared using the same 11 m diameter patches used for Figure 2. The color scale shows the base 10 logarithm of the number of bins contributing at each  $d$ - $R$  pair. The results for the (top) level ice and (bottom) deformed ice fractions are shown separately. Also plotted is the modeled relation using appropriate densities (white curve), with a fixed snow thickness of 30 cm (Figure 4, top) and 42 cm (Figure 4, bottom, white curve) and with typical ice porosities and 52 cm snow thickness (Figure 4, bottom, gray curve). Yellow curves show the effect of the expected laser freeboard measurement error (not isostatically compensated). Light blue curves show the effect of isostatically compensated snow thickness variability for snow thicknesses between 20 and 70 cm (Figure 4, top) and 27–82 cm (Figure 4, bottom).

thickness to the surface elevation there. The modal value of  $R$  over the whole data set is 3.4, with the level FY ice areas dominating this contribution. The inset cumulative distribution function (CDF) shows that approximately 50% of the data lie more than  $R \pm 1$  from the mode ( $R = 2.4$  intercepts the curve at 22%,  $R = 4.4$  at 72%). Such large departures from the level ice  $R$  clearly show that much of the region is not in the point-to-point isostatic balance that homogenous material properties would suggest. We postulate that the

high  $R$  values lie dominantly in the deformed ice areas and examine the variation of  $R$  with draft in section 3.3.

### 3.3. $R$ Versus Draft

[34] The relation between draft and  $R$  is displayed in Figure 4, again split into level ice (Figure 4, top) and deformed ice (Figure 4, bottom) fractions and calculated taking median values for 11 m diameter patches. The color scale again shows the base 10 logarithm of the number of bins, this time with any particular  $\langle$ draft- $R$  pairing. As previously suggested by Figure 2, the majority of level ice points are clustered around the FY level ice draft value of 1.65 m, with a large variation in  $R$ : a significant number of points are encountered with ratios between 2 and 5 for this draft. Also as seen in Figure 2, a second core of values is clustered around 40 cm draft (refrozen leads), with  $R$  values of around 1.5. Evident in this plot is a general increase of  $R$  with draft.

[35] The white curve shows the expected relation between draft and  $R$ , eliminating ice freeboard from the isostatic relation (equation (1)) and expressing it in terms of densities, draft and snow thickness only:

$$R = \frac{\rho_i d}{d(\rho_w - \rho_i) + h_s(\rho_i - \rho_s)} \quad (3)$$

[36] Fixed values are used for ice density ( $918 \text{ kg m}^{-3}$ ), snow density ( $240 \text{ kg m}^{-3}$ ) and snow thickness, as before. The contribution of (1) snow thickness variability and (2) laser measurement error to the observed variability of  $R$  was then assessed. For each draft, the snow thickness was varied and equation (3) recalculated, to give an isostatically compensated error. Results are shown as the light blue curves. Snow thicknesses between 20 and 70 cm (Figure 4, top) cover most of the observed variability ( $3 < R < 6$ ). The effect of the laser measurement error of 15 cm RMS per bin was assessed by adding/subtracting that error without recalculating the isostatic relation. If the error is independent between bins, then the error for each patch is reduced by the square root of the number of bins making up the patch (73 for an 11-bin diameter patch), giving 1.8 cm error in this case. The yellow curves plotted in Figure 4 (top) indicate that such an error is rather small, though in fact the error is unlikely to be completely independent from bin to bin.

[37] Figure 4 (bottom) shows the  $\langle$ draft- $R$  relation for deformed ice, also using 11 m diameter patches. The data, especially in the core region centered on 2 m draft, are much better aligned with the modeled curve, which uses the optimum fixed snow thickness of 42 cm (no porosity, white curve) and 52 cm (gray curve, using typical porosity values above and below water). 17% of patches have  $R$  values more than twice that seen over level ice. The blue curves plot isostatically compensated snow thickness between 27 and 80 cm, which include the majority of data. There are a significant number of points at  $R > 6$ , however, which may be attributed either to a reduced snow load over deformed ice, reflecting the often bare ice nature of ridge crests; to a decreased effective density of the ice-snow composite in deformed features, as evoked by the inverse thickness-density relation of Ackley *et al.* [1976]; or, probably dominantly, due to the fact that deformed features tend to be much more extensive underwater than above.

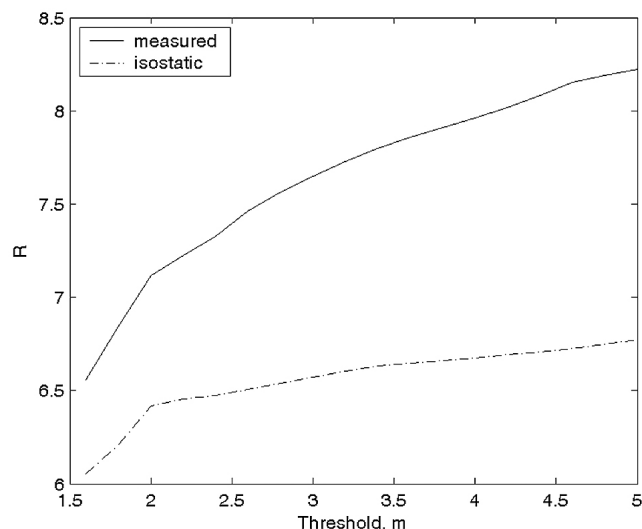


**Figure 5.**  $R$  values over the FY pressure ridge, calculated as “measured” (mean draft/mean surface elevation) and “predicted” (draft calculated from surface elevation by isostasy) for various threshold values of draft used to define the ridge keel.

### 3.4. FY Ridge

[38] We investigate this last issue, the extensive nature of underwater deformed features and therefore the difficulty in estimating their contribution from surface measurements, by isolating and examining the FY pressure ridge, comparing the total underwater ice volume that would be predicted by isostasy from the laser data with the volume actually measured by the AUV sonar.

[39] The coincident data set was cut down to an area of  $76 \times 136$  m around the ridge and the ridge further delimited by removing points less than a given draft threshold. We calculate the measured  $R$  value over the thresholded region as the sum of drafts in the  $1 \times 1$  m bins (i.e., ice volume underwater), divided by the total volume in the same region as seen by the laser (i.e., the ice volume above water). This is equivalent to the mean  $R$  value over the ridge. We compare this figure to the  $R$  value predicted from the surface elevation by isostasy, according to equation (1), for a range of threshold drafts, in Figure 5.

[40] Examining the thresholded regions by eye suggests that a threshold of 3.0 m is most appropriate in this case, approximately double the surrounding level ice thickness of 1.65 m. Over the whole ridge area, the measured  $R$  value is 7.7 at this threshold, while isostasy would predict a value of 6.6. The discrepancy increases with greater thresholds, as the slopes leading up to the keel maximum are excluded from the below-water calculation, while the significant ridge sail (which is centered above the keel in this case) remains to contribute to the above-water component. Thus, the isostatic relation tends to significantly underestimate the actual draft in the ridge area. Taking representative porosities for the ridge keel (30%) and sail (20%) into account shifts the overall  $R$  values for the ridge to 6.5 (measured) and 5.8 (predicted), at a threshold of 3.0 m.

### 3.5. Regionally Averaged $R$

[41] It is clear that the size of the patch within which we calculate statistical values plays an important part in constraining the measured values to a workable (surface elevation  $\rightarrow$  thickness) relation, trading spatial resolution for accuracy in ice thickness. We therefore examine how the descriptive statistics change as the averaging scale (footprint) is increased.

[42] The median within circular patches is therefore calculated, from full  $1 \times 1$  m resolution to 300 m diameter patches encompassing the whole data set, similar in area to the footprint of CryoSat-2’s radar altimeter in sea ice mode [Wingham *et al.*, 2006]. As before, a circular patch of a given diameter is run over the data at half-radius increments in both  $x$  and  $y$  directions. For surface elevation, we also calculate the result using the minimum value within each patch, as recent work suggests that CryoSat retrievals are largely determined by the thinnest ice within a footprint [Tonboe *et al.*, 2010]. ICESat is assumed to return the mean surface elevation within a footprint over snow covered surfaces [Kwok *et al.*, 2007] and we calculate the mean within each patch accordingly. We also calculate the mode (both within a patch and mode of all modal values). In each case the  $R$  value is calculated using the median draft value within the corresponding patch, since comparing methods with this data set, it was found that the median gives the most stable measure of  $R$  at any scale. Figure 6 presents the results, again split into level ice (Figure 6, top) and deformed ice (Figure 6, bottom) fractions.

[43] For level ice, the mean and median relations hardly deviate from their full-resolution value of  $R = 3.4$  at any scale, reflecting the dominant nature of level FY ice, with its relatively tightly constrained  $R$  values, in this data set. The ICESat-like response (mean surface elevation) is particularly stable, deviating by less than  $\pm 0.1$  over the whole range, while the median rises slightly to 3.6 at large scales. The interquartile range for this solution (plotted in gray) more than halves over the same scale range (25th and 75th percentile ranges marked). Modal values diverge to  $R = 4.1$  at the full data set size. The (median draft–minimum surface elevation) curve (not plotted) quickly outstrips reasonable  $R$  values, reaching  $R = 43$  for the largest patch. Since a single  $1 \times 1$  m bin is unlikely to greatly perturb CryoSat returns, we instead calculate the surface elevation of the lowest 10% and lowest 25% of bins within a patch.  $R$  values for both solutions are significantly higher than either the mean or median results, reaching  $R = 4.3$  and 5.2, respectively, at the largest scale.

[44] At averaging scales of 11 m and above, the mode and mean diverge from the median value, the mode increasing while the mean drops. Examining probability density functions of the  $R$  population at various scales shows the reason for this: Larger footprints allow the laser to resolve thin ice patches, splitting the distribution of  $R$  values into two peaks and eliminating  $R$  values between 1.8 and 2.8 from the statistics. For level ice, the scale dependence of  $R$  is thus largely dependent on the characteristics of the laser measurement, at least for these data which are dominated by the  $R$  values for two ice types: FY level ice and thin, refrozen leads.

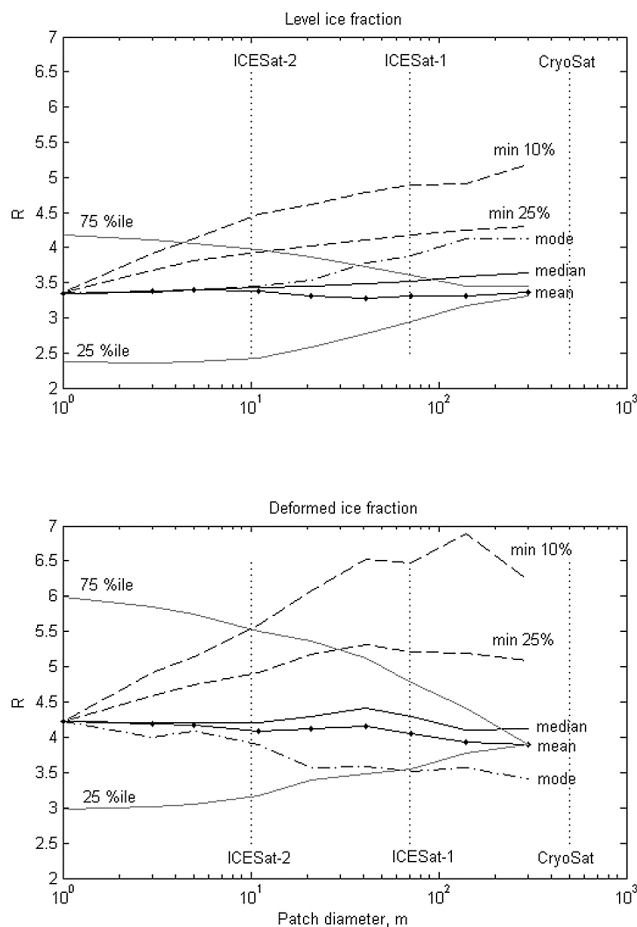


**Figure 6.** Regionally averaged  $R$  values, for (top) level ice and (bottom) deformed ice over circular patches ranging from 1 to 501 m diameter. Surface elevation values are calculated as (1) the mode, (2) the mean, (3) the median, (4) the minimum 10%, and (5) the minimum 25% of values within a patch. Draft values are calculated as the median of bins within a patch in all cases.  $R$  values are then calculated as the median of all patch values, reducing the data to a single value for each scale. The 25% and 75% interquartile ranges are marked for the mean solution (dashed lines). Typical ICESat-2, ICESat-1, and Cryosat footprints are indicated as vertical dotted lines.

[45] The deformed ice fraction (Figure 6, bottom), exhibits more variability, as would be expected. The mean and median solutions exhibit similar behavior, being rather stable around the full resolution value of 4.2, with the mean tracking slightly lower than the median. Interquartile range is significantly larger than for level ice, at  $3 < R < 6$  at full resolution (compare  $2.4 < R < 4.2$  for level ice).

[46] In contrast to level ice, the modal solution is lower than either the mean or median, dropping to 3.4 at the largest scale: the probability density function becomes more peaked, losing data on the upper tail as the mode shifts to lower  $R$ s. No secondary peak emerges due to laser resolution issues, in contrast to the level ice fraction. The minimum 10% and 25% solutions are predictably much less

stable than for level ice, rising to maxima of 6.9 and 5.3, respectively.

### 3.6. An Isostatic Scale?

[47] While examining the variation with patch diameter, it is tempting to search for an “isostatic scale,” some footprint size at which the measured surface elevation and draft approach the expected isostatic relation. With reference to Figure 2, this is equivalent to finding a patch diameter at which the population of  $\langle \text{draft} - \text{surface elevation} \rangle$  bins collapses onto the straight line fit.

[48] Accordingly, we calculate  $\overline{\Delta d}$ , the mean draft error from isostasy (equation (2)), at various scales. Since we can find a snow thickness at each scale that gives zero error (taking account of the sign of the calculated draft error), we now take the absolute (unsigned) draft error, using a fixed snow thickness for level ice (30 cm), deformed ice (42 cm) and deformed ice with typical porosities (52 cm). Those optimum thicknesses, determined in section 3.2 for 11 m diameter patches, remain constant across the averaging scales examined here.

[49] Figure 7 plots the variation of this  $\overline{\Delta d}_{\text{abs}}$  for various patch diameters, for level, deformed, and porous deformed ice separately. The level ice mean error drops in a straight line fashion (asymptotically on a linear scale), bottoming out at approximately 0.44 m at patch diameters of 70 m and above, suggesting that 70 m is the length scale over which the level ice cover achieves isostatic balance. The deformed ice fraction has a significantly higher mean draft error ( $\sim 1.7$  m) at small scales, as might be expected, again dropping in an asymptotic manner, with a larger linear gradient than the level ice fraction. Deformed ice apparently does not reach its asymptote at the scales examined here, though the

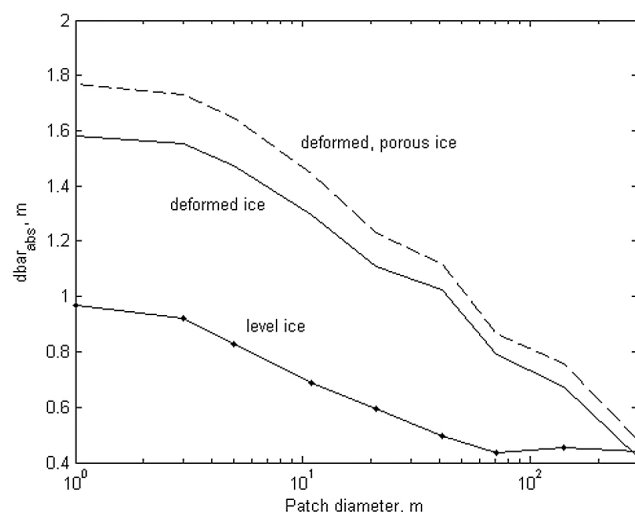


**Figure 7.** The unsigned (absolute) mean draft deviation from isostasy ( $\overline{\Delta d}_{\text{abs}}$ ), in meters, plotted across the range of available scales. Level and deformed ice are calculated separately, and the deformed ice values are also calculated using typical porosity values for above- and below-water components.

value at the largest scale (300 m) is very similar to that achieved for the level ice fraction.

#### 4. Discussion and Conclusions

[50] The area surveyed appears to be rather typical of conditions in the spring Beaufort Sea, with level FY ice thickness similar to that seen in previous studies [Melling and Riedel, 1995; Melling et al., 1993], similar maximum keel depths for the FY ridge feature [Melling et al., 1993] and typical snow thickness, though the measured snow density is low compared to the climatology of Warren et al. [1999], which ranges from  $250 \text{ kg m}^{-3}$  in September to  $320 \text{ kg m}^{-3}$  in May. The proportion of deformed ice (45% by area) is at the lower limit in relation to previous Beaufort Sea ULS profiles, which ranged from 45% to 70% [Melling and Riedel, 1995].

[51] The very high resolution data show that the airborne laser profilometer requires averaging over larger patches (11 m) to resolve the thin refrozen leads from the level FY ice. Correlation with the corresponding sonar ice draft is reasonably good at these scales, at  $r_s^2 = 0.70$ .  $R$  is highly variable even over level ice, though the most common values of draft and surface elevation lie on the expected isostatic relation with a mean snow depth of 30 cm, which reflects the in situ measurements.

[52] There is a general increase in  $R$  with ice thickness, as noted by previous investigators, and a strong tendency for the data to display lower  $R$  values than the modeled curve over level ice. This can be attributed either to a dominantly positive snow thickness anomaly or, equivalently, a lower composite material density ( $\rho_m$ ) than the measured fixed ice density would suggest. No evidence of thickness-dependent material density could be found, however, in contrast to earlier work by Ackley et al. [1976] and Kovacs [1997]. For the current data set, material densities present a wide range of values at the two dominant drafts, which remained true whether the values were calculated at full resolution or over larger patch sizes. This finding agrees with the conclusions of Wadhams et al. [1992] and Forsstrom et al. [2011] whose calculated material densities were consistent over their study regions.

[53] Over deformed ice, the apparent material density was in fact higher, opposite to that suggested by Ackley et al. [1976] and Kovacs [1997]. This can be attributed both to the fact that deformed ice features tend to be wider underwater than above, as well as to the highly porous nature of the young FY deformed ice, where seawater in the open pore spaces significantly increases the overall features' apparent density when its envelope is measured, as done by the sonar. These factors result in the highest  $R$  values occurring over deformed ice. The  $\langle R\text{-draft} \rangle$  relation follows the modeled isostatic curve more closely over deformed ice than for the complete data set, since variations in  $R$  are more closely tied to ice thickness over deformed ice, as opposed to the snow thickness variability which apparently dominates the variability of  $R$  over level ice in these data.

[54] Examining how  $R$  changes with footprint size and averaging method shows it to be rather stable at over all scales examined, from full-resolution  $1 \times 1 \text{ m}$  bins to a patch size covering the complete data set, at least where the

mean and median of values within each patch are used. For level ice, the dominance of FY level ice in these data accounts for this: this ice type is sufficiently extensive and homogenous that it matters little what footprint size is used. The result is perhaps more surprising for deformed ice, whose magnitude of variation of mean and median with scale is very similar to that seen for level ice ( $\sim 0.3$ ), though the interquartile range is nearly three times the spread of level ice values: the PDF of deformed ice  $R$  values becomes more peaked with increasing scale, but does not change in its essential character. The PDFs of  $R$  for level ice change considerably, however, due to the averaged laser measurements being able to resolve the thin ice peak at patch sizes above 11 m, and results in the level ice mode evolving in the opposite sense (i.e., increasing) to the deformed ice fraction.

[55] The stated characteristic of the ICESat instrument in measuring the mean surface elevation within its 70 m diameter footprint is shown to slightly underestimate  $R$  (overestimate surface elevation) for these data, compared to the median solution. Surface elevations in a similar region of the Beaufort Sea were estimated by ICESat as 27 cm over FY ice [Kwok et al., 2007], versus 42 cm in the current data (laser) and 40 cm measured on the ground, though this was slightly earlier in the season (February/March) than this study. Comparisons with airborne underflights have also shown ICESat to generally underestimate the surface elevation, with the bias dependent on sea ice conditions and ice thickness. In heavy ice conditions (heavily deformed, dominantly multiyear ice), ICESat was shown to underestimate surface elevation by up to 37 cm [Skourup and Forsberg, 2006]. In areas of thinner ice with more open leads, ICESat surface elevation heights were underestimated by 9 cm, and in areas of flat ice with many open leads, the bias was less than 2 cm [Kurtz et al., 2008]. Slight underestimation was also found in comparison to moored upward looking sonar drafts [Kwok and Cunningham, 2008].

[56] The CryoSat simulation, taking a surface elevation corresponding to the minimum 10% or 25% of values within a patch, is less successful, significantly overestimating  $R$  at representative footprint sizes (e.g.,  $R > 6$  for minimum 10% values over deformed ice and  $R > 5$  over level ice). The mechanism by which the thinnest ice dominates the CryoSat return is not a simple "percentage minimum" as used in this simulation, however, but is dependent on surface roughness [Tonboe et al., 2010, p. 64]: "The high backscatter magnitude from the thinnest ice within the footprint largely determines the elevation of the effective scattering surface" and has a significant effect down to very low percentage area coverage of the thinner ice type. Though it should be borne in mind that the CryoSat radar penetrates the snow layer, unlike the laser measurements considered here, it is clear that such characteristics will significantly affect CryoSat's ability to correctly report ice thickness over the varied ice terrain which forms the vast majority of Arctic pack ice. Such measurements will require careful ground truthing across a variety of regions and seasons.

[57] The mean draft error between that predicted by isostasy from surface elevation measurements and the measured draft value fell asymptotically with increasing averaging scale, for both level and deformed ice fractions.

For level ice an isostatic length scale of 70 m was suggested, since the error did not reduce further at higher scales. No minimum value was observed for deformed ice, however, even at 300 m scale, suggesting that the isostatic length scale for deformed ice is longer than the current data set can resolve. Literature figures for the isostatic length scale of Beaufort Sea ice (mixed level and deformed ice fractions) are in this range: *Melling et al.* [1993] found a similarly sized sample of Beaufort Sea ice to be close to balance on a scale of 235 m. We note that a fixed snow thickness (as used to calculate  $\overline{\Delta d}_{\text{abs}}$ ) is not likely over the deformed ice fraction, particularly since a nonnegligible portion of the data has an ice + snow surface elevation less than the best fit values of 42 and 52 cm and negative ice freeboards are uncommon in the Arctic.

[58] It should be emphasized that the understanding gained here is in no small measure due to the in situ measurements of density (ice, snow and seawater) and thickness (ice and snow) carried out by the various teams at the SEDNA camp, which allow the expected isostatic relation to be constrained. Such a program should be considered essential to future coincident surveys. The current study would have benefited greatly from detailed measurements of the snow-ice interface, either from aircraft-borne radar altimeter overflights, or simply more detailed snow thickness measurements in a dense grid over the study area. Snow stratigraphy measurements would be also be beneficial, allowing radiometric modeling of expected radar altimeter returns.

[59] These data are, of course, only from one region at one time. If we are to properly understand the response of long-term, spaceborne, measurement strategies, it will be important to repeat such coincident surveys in other regions and seasons.

[60] **Acknowledgments.** This work was a collaborative effort between the DAMOCLES project (Developing Arctic Modelling and Observation Capacities for Environmental Science) [*Gascard et al.*, 2008]; grant 018509 of the Global Change and Ecosystems call under the Sixth Framework Programme of the European Union; and the SEDNA project [*Hutchings et al.*, 2008], grant ARC-0612527 to the University of Alaska Fairbanks from the U.S. National Science Foundation. We thank Richard Yeo and Eggert Magnusson (of Hafmynd Ehf) for their technical assistance during the fieldwork and Bruce Elder for the EM-31 snow thickness measurements. We also thank the two anonymous reviewers for their insight and helpful comments which greatly improved the final manuscript.

## References

- Ackley, S. F., W. D. Hibler III, F. K. Kugzruk, A. C. Kovacs, and W. F. Weeks (1976), Thickness and roughness variations of Arctic multiyear sea ice, *Rep. 76-18*, 25 pp., Cold Reg. Res. and Eng. Lab., Hanover, N. H.
- Andreas, E., M. Lange, S. Ackley, and P. Wadhams (1993), Roughness of Weddell sea ice and estimates of the air-ice drag coefficient, *J. Geophys. Res.*, *98*(C7), 12,439–12,452.
- Bowen, R. G., and D. R. Topham (1996), A study of the morphology of a discontinuous section of a first year Arctic pressure ridge, *Cold Reg. Sci. Technol.*, *24*, 83–100, doi:10.1016/0165-232X(95)00002-S.
- Comiso, J. C., P. Wadhams, W. B. Krabill, R. N. Swift, J. P. Crawford, and W. B. I. Tucker (1991), Top/bottom multisensor remote sensing of Arctic sea ice, *J. Geophys. Res.*, *96*(C2), 2693–2709, doi:10.1029/90JC02466.
- Davis, N., and P. Wadhams (1995), A statistical analysis of Arctic pressure ridge morphology, *J. Geophys. Res.*, *100*(C6), 10,915–10,925.
- Doble, M. J., P. Wadhams, A. Forrest, and B. E. Laval (2009), Through-ice AUV deployment: Operational and technical experience from two seasons of Arctic fieldwork, *Cold Reg. Sci. Technol.*, *56*, 90–97, doi:10.1016/j.coldregions.2008.11.006.
- Forsberg, R., and S. Kenyon (2004), Gravity and geoid in the Arctic region the northern gap now filled, paper presented at *GOCE Workshop*, Eur. Space Agency, Frascati, Italy.
- Forsberg, R., and H. Skourup (2005), Arctic Ocean gravity, geoid and sea-ice freeboard heights from ICESat and GRACE, *Geophys. Res. Lett.*, *32*, L21502, doi:10.1029/2005GL023711.
- Forsstrom, S., S. Gerland, and C. A. Pedersen (2011), Sea ice and snow densities and hydrostatic equilibrium assumption from in situ measurements in Fram Strait, Barents Sea and Svalbard coast, *Ann. Glaciol.*, *57*, 216–270.
- Francois, R. E. (1977), High resolution observations of under-ice morphology, *Rep. 7712*, 30 pp., Appl. Phys. Lab., Univ. of Wash., Seattle.
- Gascard, J.-C., et al. (2008), Exploring Arctic Transpolar drift during dramatic sea ice retreat, *Eos Trans. AGU*, *89*(3), 21–28, doi:10.1029/2008EO030001.
- Haas, C., S. Hendriks, and M. J. Doble (2006), Comparison of the sea ice thickness distribution in the Lincoln Sea and adjacent Arctic Ocean in 2004 and 2005, *Ann. Glaciol.*, *44*, 247–252, doi:10.3189/172756406781811781.
- Hutchings, J., et al. (2008), Role of ice dynamics in the sea ice mass balance, *Eos Trans. AGU*, *89*(50), 515, doi:10.1029/2008EO500003.
- Hvidegaard, S. M., and R. Forsberg (2002), Sea-ice thickness from airborne laser altimetry over the Arctic Ocean north of Greenland, *Geophys. Res. Lett.*, *29*(20), 1952, doi:10.1029/2001GL014474.
- Hvidegaard, S. M., R. Forsberg, and H. Skourup (2006), Sea ice thickness estimates from airborne laser scanning, in *Sea Ice Thickness: Past, Present and Future*, edited by P. Wadhams and G. Amanatidis, pp. 193–206, Eur. Union, Brussels.
- Kovacs, A. C. (1997), Estimating the full-scale flexural and compressive strength of first-year sea ice, *J. Geophys. Res.*, *102*(C4), 8681–8689, doi:10.1029/96JC02738.
- Kovacs, A. C., W. F. Weeks, S. F. Ackley, and W. D. Hibler III (1973), Structure of a multi-year pressure ridge, *Arctic*, *26*(1), 22–31.
- Krabill, W. B., R. H. Thomas, C. F. Martin, R. N. Swift, and E. B. Frederick (1995), Accuracy of airborne laser altimetry over the Greenland ice sheet, *Int. J. Remote Sens.*, *16*(7), 1211–1222, doi:10.1080/01431169508954472.
- Kurtz, N. T., T. M. Markus, D. J. Cavalieri, W. B. Krabill, J. G. Sonntag, and J. Miller (2008), Comparison of ICESat lidar data with airborne laser altimeter measurements over Arctic sea ice, *IEEE Trans. Geosci. Remote Sens.*, *46*(7), 1913–1924, doi:10.1109/TGRS.2008.916639.
- Kwok, R., and G. F. Cunningham (2008), ICESat over Arctic sea ice: Estimation of snow depth and ice thickness, *J. Geophys. Res.*, *113*, C08010, doi:10.1029/2008JC004753.
- Kwok, R., G. F. Cunningham, H. J. Zwally, and D. Yi (2007), Ice, Cloud and land Elevation Satellite (ICESat) over Arctic sea ice: Retrieval of freeboard, *J. Geophys. Res.*, *112*, C12013, doi:10.1029/2006JC003978.
- Lepparanta, M., and R. Hakala (1992), The structure and strength of first-year ice ridges in the Baltic Sea, *Cold Reg. Sci. Technol.*, *20*, 295–311, doi:10.1016/0165-232X(92)90036-T.
- Maslowski, W., and W. H. Lipscomb (2003), High-resolution simulations of Arctic sea ice, *Polar Res.*, *22*(1), 67–74, doi:10.1111/j.1751-8369.2003.tb00097.x.
- Melling, H., and D. A. Riedel (1995), The underside topography of sea ice over the continental shelf of the Beaufort Sea in the winter of 1990, *J. Geophys. Res.*, *100*(C7), 13,641–13,653.
- Melling, H., D. R. Topham, and D. Riedel (1993), Topography of the upper and lower surfaces of 10 hectares of deformed sea ice, *Cold Reg. Sci. Technol.*, *21*, 349–369, doi:10.1016/0165-232X(93)90012-W.
- Skourup, H., and R. Forsberg (2006), Sea ice freeboards from ICESat—A comparison to airborne lidar measurements, in *Arctic Sea Ice Thickness: Past, Present and Future*, edited by P. Wadhams and G. Amanatidis, pp. 82–92, Eur. Union, Brussels.
- Timco, G. W., and R. P. Burden (1997), An analysis of the shapes of sea ice ridges, *Cold Reg. Sci. Technol.*, *25*, 65–77, doi:10.1016/S0165-232X(96)00017-1.
- Timco, G. W., and W. F. Weeks (2010), A review of the engineering properties of sea ice, *Cold Reg. Sci. Technol.*, *60*, 107–129, doi:10.1016/j.coldregions.2009.10.003.
- Tonboe, R. T., L. T. Pedersen, and C. Haas (2009), Simulation of the satellite radar altimeter sea ice thickness retrieval uncertainty, *Cryosphere Discuss.*, *3*, 513–559, doi:10.5194/tcd-3-513-2009.
- Tonboe, R. T., L. T. Pedersen, and C. Haas (2010), Simulation of the Cryosat-2 satellite radar altimeter sea ice thickness retrieval uncertainty, *Can. J. Remote Sens.*, *36*(1), 55–67, doi:10.5589/m10-027.
- Wadhams, P., and M. J. Doble (2008), Digital terrain mapping of the underside of sea ice from a small AUV, *Geophys. Res. Lett.*, *35*, L01501, doi:10.1029/2007GL031921.

- Wadhams, P., W. B. I. Tucker, W. D. Krabill, R. N. Swift, J. C. Comiso, and N. R. Davis (1992), Relationship between sea ice freeboard and draft in the Arctic Basin, and implications for ice thickness monitoring, *J. Geophys. Res.*, 97(C12), 20,325–20,334.
- Warren, S. G., I. G. Rigor, N. Untersteiner, V. F. Radionov, N. N. Bryazgin, Y. I. Aleksandrov, and R. Colony (1999), Snow depth on Arctic sea ice, *J. Clim.*, 12(6), 1814–1829, doi:10.1175/1520-0442(1999)012<1814:SDOASI>2.0.CO;2.
- Webster, R., and M. A. Oliver (2007), *Geostatistics for Environmental Scientists*, 315 pp., John Wiley, Chichester, U. K., doi:10.1002/9780470517277.
- Weeks, W. F. (2010), *On Sea Ice*, 600 pp., Univ. of Alaska Press, Anchorage.
- Wilkinson, J. P., P. Wadhams, and N. E. Hughes (2007), Modelling the spread of oil under fast sea ice using three-dimensional multibeam sonar data, *Geophys. Res. Lett.*, 34, L22506, doi:10.1029/2007GL031754.
- Wingham, D. J., et al. (2006), CryoSat: A mission to determine the fluctuations in the Earth's land and marine ice fields, *Adv. Space Res.*, 37, 841–871, doi:10.1016/j.asr.2005.07.027.
- 
- M. J. Doble, UPMC, LOV, UMR 7093, UPMC, Université Paris 06, Observatoire Océanologique, F-06234 Villefranche sur Mer, France. (doble@obs-vlfr.fr)
- C. A. Geiger, Geography Department, College of Earth Ocean and Environment, University of Delaware, Newark, DE 19716, USA.
- H. Skourup, Division of Geodynamics, National Space Institute, Juliane Maries Vej 30, DK-2100 Copenhagen Ø, Denmark.
- P. Wadhams, Department of Applied Maths and Theoretical Physics, University of Cambridge, Wilberforce Road, Cambridge CB3 0WA, UK.